Fabrication of a binder-free lithium manganese oxide cathode for secondary Li - Ion batteries

C. Bubulinca [1*], I. Sapurina [1], N. E. Kazantseva [1], J. Vilcakova [1], Q. Cheng [1,2], P. Saha [1]

1 Centre of Polymer Systems, Tomas Bata University in Zlin, Tr. T. Bati 5678, Zlin, 760 01, Czech Republic

2 Key Laboratory for Ultrafine Materials of Ministry of Education, School of Material Science and Engineering, East China University of Science and Technology, Shanghai, China 200237, China.

Address correspondence to E-mail: bubulinca@utb.cz

Abstract

The binder-free technology is used to produce flexible self-standing cathodes for secondary Li-ion batteries containing commercial materials: lithium manganese oxide ($LiMn_2O_4$) and multiwall carbon nanotubes. The fragmentation of commercial $LiMn_2O_4$ by short time ball-milling with low energy intensities allows one to reduce the particle size from tens of microns to the micron and submicron level, while maintaining its spinel crystal structure. Then, a stable aqueous dispersion of lithium manganese oxide and carbon nanotubes is prepared and used for processing a flexible self-standing electrode by vacuum-filtration and peeling off the dry electrode from the filter. The electrode exhibits high electrical conductivity (46 $S \cdot m^{-1}$) due to homogeneous distribution of lithium manganese oxide particles in the matrix of carbon nanotubes. Electrochemical assessment of the electrode revealed stable electrochemical characteristics during 120 cycles of voltammetry tests at 2 $mV \cdot s^{-1}$ and a specific capacity of about 80 $mAh \cdot g^{-1}$ at high current density of 0.6 mA and 110 mAh g^{-1} discharge capacity at 0.16 mA.

Key words: flexible binder-free $LiMn_2O_4$ cathode, secondary Li-Ion battery, dry ball milling

Introduction

The most problematic element in modern Li ion batteries is the cathode [1]. For this reason, new cathode materials are being actively developed and the technologies of cathode fabrication are being improved [2-4]. The new generation of cathode materials includes lithium manganese oxide (LMO) with the chemical formula $LiMn_2O_4$ [5-8]. This material has a capacity density comparable to that of the traditional $LiCoO_2$ cathode [9], but it has advantages in terms of price and safety [10]; i.e., LMO is nontoxic [9], and, moreover, manganese is very abundant in nature [10, 11]. In addition, the heat release on a $LiMn_2O_4$ cathode is ten times lower than that on $LiCoO_2$, which significantly reduces the risk of inflammation in the case of batteries with organic electrolyte [5]. For this reason, MnO_2 has been intensively studied as an electrode material in rechargeable lithium-ion batteries and asymmetric supercapacitors. Among a multitude of polymorphous forms containing MnO_2, spinel has the optimum pore structure for the intercalation/deintercalation of Li^+

ions. The spinel framework of MnO_2 provides three-dimensional tunnels for Li^+ insertion and extraction without significant changes in the unit cell volume. Reversible intercalation/deintercalation of Li^+ ion changes the composition of $Li_xMn_{2-x}O_4$ in the range $0.33 \leq x \leq 1$ and therewith changes the average oxidation state of Mn between 3.0 and 4.0 [27]. Spinel-type $LiMn_2O_4$ has the highest capacity as a cathode material for Li ion batteries [12]. The specific capacity is determined not only by lithiation/delithiation on the surface of LMO, but also by the redox processes ($Mn^{4+} \leftrightarrow Mn^{3+} \leftrightarrow Mn^{2+}$) in the bulk of the material [6]. The disadvantages of all forms of LMO, including spinel-type oxides, are low electrical conductivity (10^{-4}–10^{-6} S·m^{-1}). Therefore, to maintain the level of electrical conductivity, it is necessary to combine $LiMn_2O_4$ with an electrically conductive material, usually with carbon-based materials like mesoporous carbon, activated carbon, carbon nanotubes (CNT), and graphene, which are characterized by high specific surface area and high electrical conductivity [6].

The technology of combining the active energy storage component with carbon must ensure a uniform distribution of the components and good contact between them. A conventional method of electrode fabrication is based on the slurry-coating process. A slurry from the active material, carbon, and binder is deposited on a current collector as a planar layer [13]. Typically, polyvinylidene fluoride and polytetrafluoroethylene are used as a binder [14-17]. The binder sticks carbon and brittle inorganic material and fixes them to the current collector; however, at the same time, the binder partially blocks the transport of ions and electrons, thus reducing the active surface area of the electrode. In addition, such electrodes exhibit low flexibility due to the rigid structure [13].

The new binder-free technology of electrode fabrication is mainly based on in-situ composite preparation, when inorganic active materials are synthesized in the presence of a carbon component, or carbon is deposited on active materials using precursors [6, 18, 19]. This technology is based on chemical or electrochemical synthesis, which is not suitable for preparation of large amounts of material.

Preparation of flexible and self-standing electrodes for portable electronics needs a flexible component adapted to reversible deformation. The structure of a tangle of CNT can provide outstanding stretchability [20-22]. A matrix of this type filled with well-dispersed particles of inorganic materials forms a so-called "island-bridge" structure [23, 24]. Here, the islands of active and non-conductive inorganic material are combined with bridges of stretchable and conducting CNT.

In this work, a flexible and free-standing cathode for a Li-ion battery is fabricated by a simple binder-free method using commercially available materials such as $LiMn_2O_4$ and CNT. The aim of the work is to find an economical, energy-efficient, and environmentally friendly

solution to the energy storage problem. To this end, we simplify the manufacturing technology of the cathode, which includes the following steps: (i) ball milling to increase the specific surface of the LMO and to reduce the number of structural defects, (ii) ultrasound assisted dispergation of LMO and CNT in aqueous Triton X-100 solution, and (iii) direct deposition of the dispersion on a nano-porous polymeric membrane by vacuum filtration.

2. Materials and methods

2.1. Materials

Sintered $LiMn_2O_4$ with spinel-type structure was purchased from MTI Co. Ltd, where it was produced by heat treatment (750°C in air) of a mixture of lithium salt (e.g. $CH_3COOLi \times 2H_2O$) and manganese oxide.

Multiwall carbon nanotubes with length of about 1.5 μm and diameter of about 10 nm were purchased from Nanocyl Company, where they are produced by chemical vapor deposition method.

Triton X-100 - poly(ethylene glycol) p-isooctyl-phenyl ether from Sigma Aldrich was used as a surfactant for preparation of aqueous dispersions.

Polyvynilidene fluoride (PVDF) membranes with a pore size below 200 nm and a total volume of pores greater than 70% were purchased from Millipore Corporation (USA).

2.2. Ball-milling procedure

As received LMO powder was milled in LAB WIZZ 320 MICRO BALL MILL using stainless steel balls of 30 mm diameter. The ball-to-LMO powder mass ratio was 32.6/4 g. The rotation speed was set to 300 rpm, and the milling time was ranged from 20 to 50 minutes (20, 30, 40 and 50 minutes: samples LMO20, LMO30, LMO40 and LMO50, respectively).

2.3. Fabrication of a binder-free self-standing cathode

LMO (178 mg) and CNT (23 mg) with component ratio of 87/13 wt.% were dispersed in 50 ml of aqueous solution of Triton X-100 (1 wt. %) and ultrasonicated for 30 minutes until a stable blue-violet colloid was formed. Vacuum filtration of the colloid and washing of the sediment with water to remove Triton X-100 was carried out on a 2.5-cm-diameter PVDF membrane. After air drying, the LMO/CNT layer was peeled off from the membrane, washed with deionized water and dried at 110° C for 12 h.

2.4. Characterization

The LMO particle size and particle size distribution were determined by the laser diffraction method (Malvern Mastersizer 3000), in which the angular variation in the intensity of light scattered from the particles was measured and the data obtained were used to calculate the particle size on the basis of the Mie light scattering theory. The particle size is reported as a volume equivalent sphere diameter (D_v) [25].

The morphology of the materials was studied by a scanning electron microscope (FE-SEM, FEI T12) operating at 120 kV.

The crystal structure of the LMO was analyzed with the help of X-ray diffraction techniques (XRD, Advance D8, Bruker) with Cu-Kα radiation.

Raman spectroscopy was conducted to determine the structural changes in LMO after fragmentation. To this end, a Nicolet DXR (Thermo Scientific) dispersive Raman microscope with a He-Ne laser (514 nm) was used in the range of $200 - 800$ cm^{-1}.

The DC conductivity was measured by a four-point van der Pauw method on electrode samples (with a diameter of 15 mm and a thickness of about 100 µm) after peeling off from a polymeric membrane. A Keithley2410 programmable high-voltage source-meter and a Keithley 6517B electrometer/high resistance meter with a Keithley 7002 switch were employed. The measurements were carried out at ambient temperature with a current of about 10^{-6} A.

Assessment of electrochemical performance at room temperature was performed by using Autolab PGSTAT-128N potentiostat.

2.5. Electrochemical assessment

The electrochemical behavior of a binder-free self-standing electrode was studied using cyclic voltammetry (CV) at a scan rate of 2 mV·s^{-1}, galvanostatic charge-discharge using various current rates in range of 0.5-2 C, and electrochemical impedance spectroscopy (EIS). The current density was calculated according to LiMn$_2$O$_4$ theoretical capacity (1C = 148 mAh g^{-1}). Electrochemical window potential was between 0.4 and 1.2 V.

Electrochemical measurements at frequency range from 100 kHz to 10 mHz and amplitude of 5 mV were performed in a three-electrode system with an Ag/AgCl reference electrode and a platinum counter electrode in 1M Li$_2$SO$_4$.

The capacity (C) of a self-standing LMO50/CNT electrode was calculated from the CV curve by the following equation:

$$C = \int I \, dV / tv, \quad (1)$$

where C is capacity in Ah, I is the scan rate in A, V is voltage, t is total time in seconds, and v is scan rate in V/s.

The specific capacity C_S was calculated with regard to the total mass of the self-standing electrode.

3. Results and Discussion

3.1. Fabrication process of the LMO/CNT electrode material

Schematic picture of the common fabrication process of a binder-free self-standing LMO/CNT electrode is shown in figure 1.
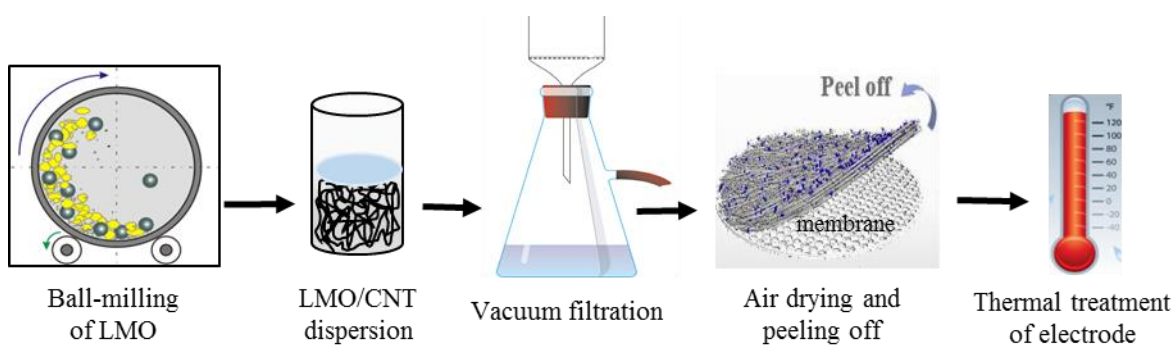

Fig. 1. Schematic illustration of the preparation process of a self-standing and flexible electrode by binder-free technology: ball-milling of LMO; ultrasound assisted dispergation of LMO and CNT in aqueous Triton X-100 solution; vacuum filtration of dispersion via PVDF membrane and removal of Tween X-100 by water; air drying of precipitate on a PVDF membrane followed by peeling off from the membrane; thermal treatment of the self-standing electrode at $110°C$ during 12h.

At the first step, the size of LMO particles is reduced by ball milling. Reducing the particle size leads to a larger surface area and shortens the diffusion length for Li^+ ions to intercalate from/into the host structure of LMO. In addition, particles of submicron size have lower mechanical stress after intercalation by Li ions. Therefore, the use of submicron-size materials for the cathode increases the charge-discharge rate and the cycling stability. However, intensive ball milling can lead to negative effects. It is reported that long-time ball milling (for more than 6 hours) and high rotation speed result in the destruction of the LMO spinel crystal structure; i.e., they give rise to defects and residual stress in the lattice that can affect the electrochemical stability of the material [26]. For this reason, we used short-time ball milling (less than 1 hour) during which the particle size of LMO and its crystal structure were controlled by XRD and Raman spectroscopy.

Reducing the particle size leads to a larger surface area and shortens the diffusion path length for Li+ ions to intercalate from/into the host structure of LMO. In addition, particles of submicron size have lower mechanical stress after intercalation by Li ions. Therefore, the use of submicron-size materials for the cathode increases the charge-discharge rate and the cycling stability. However, intensive ball milling can lead to negative effects. As reported in [26], long ball milling (more than 6 hours) results in the destruction of the LMO spinel-structure, i.e., gives rise to defects and residual stress in the lattice that can affect the electrochemical stability of the material. For this reason, we used short-time ball milling (less than 1 hour) during which the particle size distribution of LMO was verified by the laser diffraction method, and its crystal structure was controlled by XRD and Raman spectroscopy.

3.2. Morpho-structural properties

Figure 2 shows the change in the particle size distribution during the ball-milling process, which leads to an increase in the specific surface area.
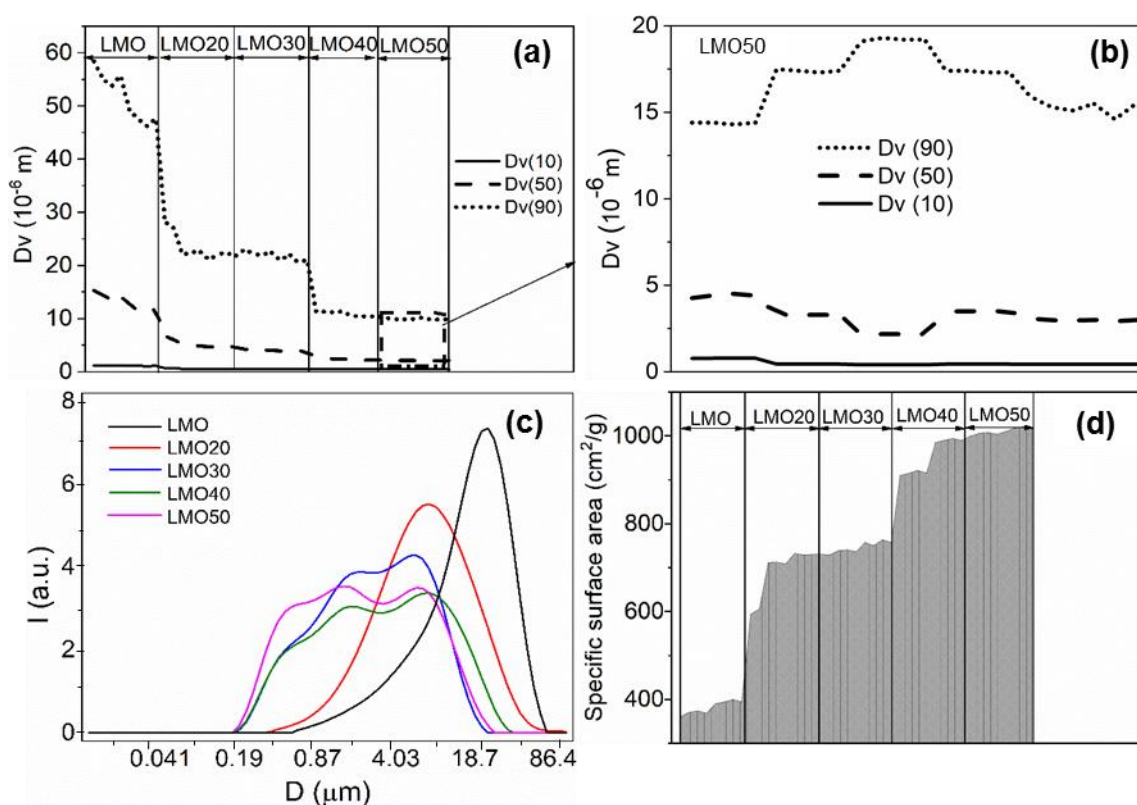
Fig. 2. LMO particles size distribution in individual fractions: (a) before ball-milling, the middle size (D_v 50), large size (D_v 10) and small size (D_v 90); (b) zooming of the LMO50 sample; (c) particle size distribution of LMO before and after ball milling. Specific surface area of particles in different samples (d).

A commercial LMO product is a powder with a wide but unimodal particle size distribution, where half of particles are 15-20 μm in size (fraction $D_v(50)$), 10% of particles are larger than 60 μm (fraction $D_v(10)$), and the mass of particles with a size of 2–3 μm is less than 10 % (fraction $D_v(90)$). With increasing milling time, the amount of small particles continuously increases, the distribution becoming multimodal and broader. Thus, after 50 minute, the particle size in all fractions decreases down to 2–3 μm in fraction $D_v(50)$, down to submicron size in fraction $D_v(90)$, and down to about 15 μm in fraction $D_v(10)$. The fragmentation of particles occurs mainly due to the destruction of large particles and leads to a 3-fold increase in the specific surface area of LMO.

The results of the of particle size distribution are confirmed by the results of electron microscopy (Fig. 3), which show that the particle size of LMO significantly decreases after ball-milling.
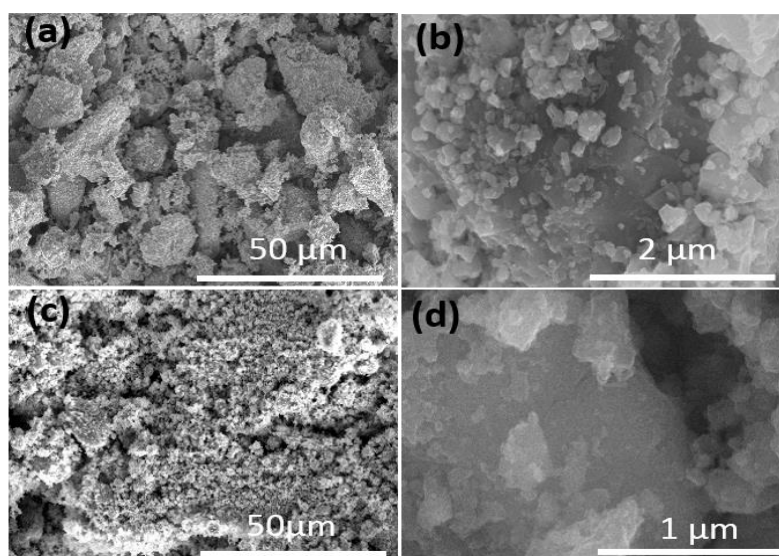
Fig. 3. SEM images of pristine LMO before (a) and after ball-milling: LMO30 (b), LMO50 (c, d).

The XRD and Raman spectra of pristine LMO and as-prepared LMO samples after ball milling are shown in Fig. 4. All peaks in the XRD spectra are well indexed to the spinel structure: the patterns are assigned to a cubic symmetry with *Fd3m* space group, and the lattice constant *a* is equal to 8.03 Å [27]. The positions of the patterns of as-prepared and pristine LMO samples are similar, but the reduction in the intensity and the broadening of the diffraction peaks provide evidence for a decrease in the particle size. To emphasis the effect of ball milling on the crystal structure, we locally magnified the (111) peaks. The position of the (111) diffraction peak is not appreciably changed. However, the intensity of the (111) peak increases, and the peak becomes broader with increasing milling time.
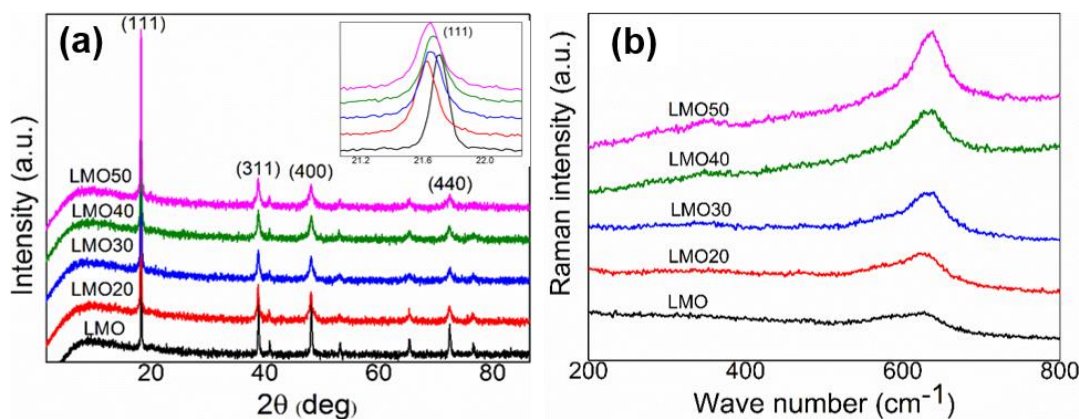
Fig. 4. XRD (a) and Raman (b) spectra of LMO before and after ball milling.

The effect of ball-milling on the local structural characteristics of LMO were studied by Raman Spectroscopy. The Raman spectra confirm the retention of the spinel structure of pristine LMO after ball-milling. The spectra of all the samples exhibit two peaks: the main peak at 650 cm^{-1}, which is attributed to the motion of oxygen atoms inside the octahedral MnO_6 unit [28-30], and a low-intensity peak at 380 cm^{-1}, which is related to the Li–O motion in the tetrahedral unit with symmetry F_{2g} {3} [31]. The intensity of the peaks increases with an increase in the milling time, which shows the enhancement of the surface area of particles.

Therefore, the investigation of the morpho-structural properties of as-prepared samples in comparison with pristine LMO confirms that short-time ball milling at low energy intensities does not change its initial spinel-type crystalline structure. It is known that low energy deposition does not introduce microstrain and defects into a crystal lattice, so that the fragmentation occurs mainly from already existing defects through the cleavage breakage process [32]. In the case of LMO, the destruction occurs mainly perpendicular to the (111) plane [26]. This feature can lead to an increase in the electrode stability against dissolution of Mn^{+2}, since dissolution occurs mainly on the (111) plane of LMO [33]. Thus, the short-time ball milling of spinel-type LMO is an expedient procedure: it allows one to obtain micron- and submicron-size particles with a threefold increased specific surface area of the active material without destroying the spinel structure and to reduce the amount of previously existing defects in the material.

3.3. Fabrication of a self-standing electrode

Another task that was solved by the fragmentation of LMO is the preparation of a homogeneous LMO50/CNT based dispersion. The smaller the particle size, the less their sedimentation, and the higher the homogeneity of the electrode material. However, the agglomeration and sedimentation of LMO and CNT occur even for small particles. To overcome this problem, we used a low molecular weight surfactant (Triton X-100). Triton X-100 is chosen

since it is successfully used as a dispersant for nano-carbon black in organic (N-metyl pyrrolidone) solvent [34] and for dispergation of CNT in distilled water [35]. Moreover, Triton X-100 shows a positive effect on the dispergation of carbon with another type of cathode material, LiFePO4, in aqueous solution [36]. It is established that the optimal concentration of Triton X-100 for CNT dispergation in water is 1.3 wt. % [35]. We prepared stable dispersions of CNT and LMO50/CNT (with component contents of 87 wt.% and 13 wt.%, respectively) in 1 wt. % of aqueous solution of Triton X-100. The SEM images of the dispersions obtained are presented in figure 5.
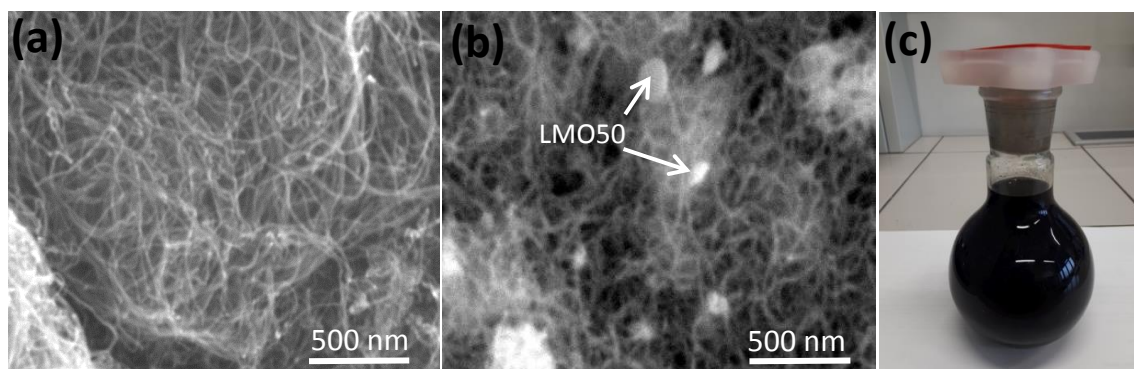

Fig. 5. SEM images of CNT (a), LMO50/CNT (b) and digital photo of LMO50/CNT dispersions in aqueous solution with 1% Triton X-100 (c).

We can see that LMO50 particles of different size (100 nm – 1 μm) are uniformly distributed in the CNT network. The stability of LMO50/CNT dispersions is good, and no sedimentation was observed after several months of storage at ambient conditions.

We used the vacuum filtration method to obtain a uniform film of a self-standing flexible electrode. To this end, we filtrated the LMO50/CNT dispersion through a PVDF membrane with a pore size of 200 nm. Therefore, only low-molecular weight components could pass through the filter. Additional intensive washing with deionized water allowed us to remove Triton X-100 residues, while a uniform LMO50/CNT layer with a thickness of about 150 μm remained on the filter. After brief drying at ambient conditions, the LMO50/CNT layer was peeled off from the PVDF membrane and treated at 110°C during 12h. The heat treatment fixed the electrode structure, thus preventing delamination and dissolution of the material. As a result, the electrode remained stable in aqueous electrolyte solutions; namely, there were no swelling and no mass loss.

Figure 6 shows a digital photo of a self-standing LMO50/CNT flexible electrode and SEM images of its surface at different magnification. The electrode consists of tightly packed micron-size fragments of sediment (Fig. 6b). Increasing the magnification of the SEM image, we can observe the "island-bridge" structure of the electrode obtained: CNT forms a network with uniformly distributed submicron-size LMO50 particles. In the "island-bridge" structure of the

LMO50/CNT electrode, the islands of LMO are connected by bridges of stretchable and conducting CNT. Even a small mass fraction of CNT (13% wt.) leads to an increase in the electrical conductivity of the electrode up to 46 S·m^{-1}. This is more than six orders of magnitude greater than the electrical conductivity of pristine LMO and corresponds to the level of electrical conductivity necessary for the electrode of a power source [37].
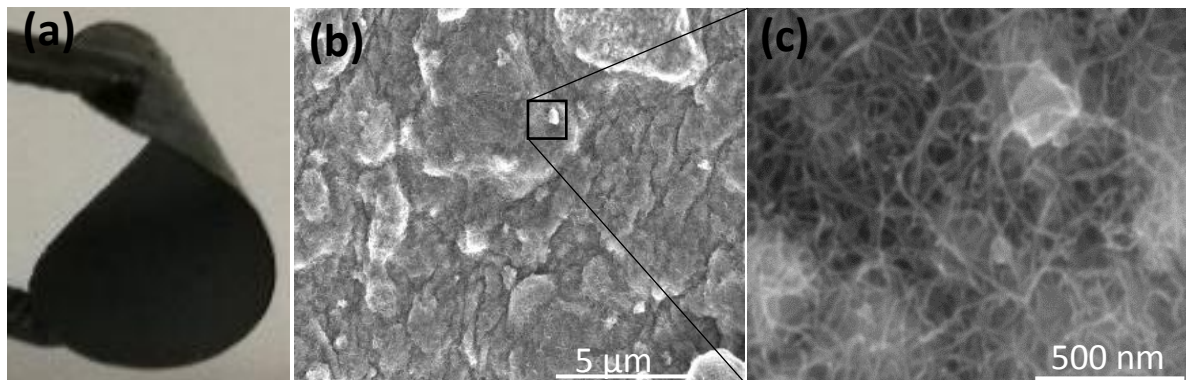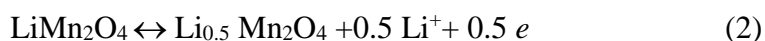

Fig. 6. Digital photo of a self-standing flexible LMO50/CNT electrode (a), SEM image of the electrode surface and bridge island matrix (b, c).

3.4. Electrochemical performance of the LMO/CNT electrode material

The electrochemical study of a self-standing flexible LMO50/CNT electrode obtained using binder-free technology was carried out in the presence of a neutral aqueous electrolyte that is used in aqueous Li-ion batteries. The aqueous Li-ion batteries are non-toxic, non-flammable and much cheaper than organic electrolyte batteries due to the simplification of the manufacturing technology and cheaper components. However, they exhibit lower capacity compared to organic Li-ion batteries [38-40] due to the reduced potential window. A typical capacity density of cathodes with aqueous electrolyte does not exceed 100 mAh·g^{-1} [40, 41].

The LMO50/CNT electrode tests were carried out in a three-electrode cell with a neutral aqueous electrolyte (1.0 M Li$_2$SO$_4$). The reference electrode was Ag/AgCl, while platinum served as counter electrode, and the self-standing flexible film of LMO50/CNT was used as a working electrode. Potential scanning was limited to 1.023 V at which water decomposition starts. Figure 7a shows the CV for the first 50 cycles at a potential scanning rate of 2 mV· s^{-1}. During the first 5−15 cycles, CV shows two peaks on both cathodic (0.6 V and 0.95 V) and anodic (0.55 and 0.9 V) sides. The redox peaks refer to the redox transitions of Mn between different valence states: Mn^{+3} / Mn^{+2} (0.6 − 0.55 V) and Mn^{+4} / Mn^{+3} (0.95 − 0.9 V) [6]. During the lithiation, a Li ion is incorporated into different tetragonal sites of the LMO spinel structure that are matched to the two-step reaction [8]:

$$LiMn_2O_4 \leftrightarrow Li_{0.5} Mn_2O_4 +0.5 \, Li^+ + 0.5 \, e \qquad (2)$$

$$LiMn_2O_4 \leftrightarrow 2MnO_2 + 0.5\,Li^+ + 0.5\,e$$

The intensity of the peaks increases, and they shift to the positive region during the cycling process, thus revealing the intensification of Faradic reactions. Changes in the CV are observed for 15 cycles, and then the CV remains unchanged for 120 cycles, indicating the high stability of the electrode material (Fig. 7a).

The capacity (C) of a self-standing LMO50/CNT electrode was calculated from equation (1). Taking into account the total mass of a self-standing electrode, we obtained the specific capacity C_S of about 80 mAh·g^{-1}.
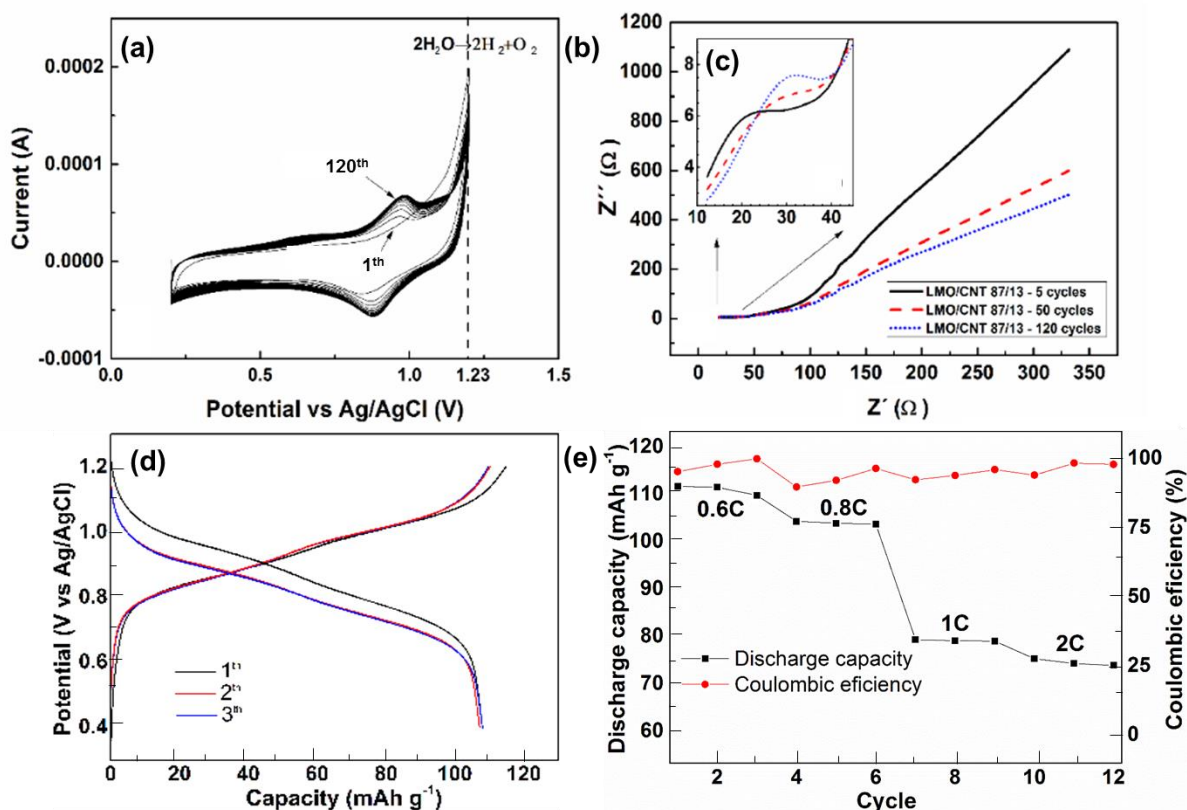
Fig. 7. Cyclic voltammetry of an LMO50/CNT self-standing electrode at a scan rate of 2 mV·s^{-1} for the first 50 cycles (a), electrochemical impedance spectra (EIS) of LMO50/CNT over the frequency range of 0.01Hz – 5·10^4 Hz after 5, 50 and 120th cycles (b) and zoom of EIS for semicircle region (c), Galvanostatic charge-discharge curve at 0.6 C (d), and discharge capacity stability at 0.6-2C for series of 3 cycles (e).

The Nyquist plots of a self-standing LMO50/CNT electrode after 5, 50 and 120th cycles are displayed in Fig. 7b. All curves contain a semicircle in the high-frequency range (Fig. 7c) and a quasi-linear part in the low-frequency range. The presence of a semicircle is due to the resistance of the electrode to charge transport. The diameter of the semicircle remains the same during 120

cycles, which indicates a good stability of the LMO50/CNT structure. The quasi-linear part at low frequency is the Warburg contribution of Li-ion diffusion through the bulk of the electrode material. The decrease in the angle of the quasi-linear Warburg part with cycling indicates an improvement in Li-ion diffusion and an increase in the charge transport rate in the LMO50/CNT electrode.

However, to quantify the amount of lithium ions, we measured galvanostatic charge/discharge cycles at different current rates: 0.16 mA (0.6 C), 0.2 mA (0.8C), 0.3 mA (1C) and 0.6 mA (2C). Figure 7d demonstrates the charge/discharge profile of a self-standing electrode at 0.6 C. One can see two semiplateaus associated with the reduction oxidation phenomenon during the charge/discharge process according to the CV data. To prove the stability and high energy density of the fabricated self-standing cathode, we repeated 3 charge/discharge cycles at different current rates: 0.6 C, 0.8 C, 1 C, and 2C. A specific discharge capacity of about 110 mAh g^{-1} was obtained at 0.6 C current rate and 77 mAh g^{-1} for 2C current rate. These results show very good discharge capacity of the cathode material obtained in comparison with other aqueous battery systems based on LMO as the active material [42]. Moreover, during the galvanostatic cycling, the variation of Coulombic efficiency is rather low, showing high reversibility of charge transport during lithiation/delithiation, which demonstrates the high stability of the cathode material structure (Fig.7e).

4. **Conclusions**

We simplified the technology for preparing a self-standing flexible cathode for rechargeable Li-ion batteries. The active material of the cathode is based on commercially available spinel-type $LiMn_2O_4$ and multiwall CNT which enhanced electrical conductivity of cathode. We have shown that the preliminary fragmentation of LMO by short-time ball-milling with low energy intensity significantly reduces the particle size without destroying its spinel structure. The fragmentation of particles to micron and submicron size ensures a 3-fold increase in the specific surface area, their uniform distribution in the CNT matrix, and a stable aqueous dispersion. This facilitates the fabrication of a flexible self-standing electrode and improves its stability and capacitive characteristics. Indeed, electrochemical tests of the cathode material in neutral aqueous electrolyte (1.0 M Li_2SO_4) revealed its stable structure resulting in a specific discharge capacity of about 110 mAh g^{-1} after first cycle at 0.6 C.

References

[1] Q. Li, J. Chen, L. Fan, X. Kong, Y. Lu, Green Energy & Environment 1, (2016). https://doi.org/10.1016/j.gee.2016.04.006

[2] W. Tang, L. Liu, Y. Zhu, H. Sun, Y. Wu, K. Zhu, Energ. Environ. Sci., 5, (2012).

[3] Q. Qu, L. Fu, X. Zhan, D. Samuelis, J. Maier, L. Li, S. Tian, Z. Li, Y. Wu, Energ. Environ. Sci., 4, (2011).

[4] W. Tang, Y. Zhu, Y. Hou, L. Liu, Y. Wu, K.P. Loh, H. Zhang, K. Zhu, Energ. Environ. Sci., 6, (2013)

[5] N.S. Choi, Z. Chen, S.A. Freunberger, X. Ji, Y.K. Sun, K. Amine, G. Yushin, L.F. Nazar, J. Cho, P.G. Bruce, Angew. Chem. Int. Ed., 51, (2012).

[6] C. M. Julien and A. Mauger, Nanomaterials, 7, (2017).

[7] X.D. Luo, Y.Z. Yin, M. Yuan, W. Zeng, G. Lin, B. Huang, Y.W. Li, S.H. Xiao, RSC Adv., 8, (2018).

[8] X. Gao, Y. Sha, Q. Lin, R. Cai, M.O. Tade, Z. Shao, J. Power Sources, (2015). https://doi.org/10.1016/j.jpowsour.2014.10.099

[9] Ch. Julien, A. Mauger, A. Vijh, K. Zaghib, Lithium Batteries, 1st edn. (Springer, Switzerland, 2016), pp. 29-68.

[10] A. Mauger, C.M. Julien, Ionics, 23, (2017).

[11] H. Manjunatha, G.S. Suresh, T.V. Venkatesha, J Solid State Electrochem. 15, (2011).

[12] O. Ghodbane, J.L. Pascal, F. Favier, ACS Appl. Mater. Interfaces, 1, (2009).

[13] L. Wen, F. Li, H.M.Cheng, Adv. Mater. 28, (2016) https://doi.org/10.1002/adma.201504225

[14] L. Qiu, Z. Shao, D. Wang, W. Wang, F. Wang, J. Wang, Carbohydrate Polymers, (2014). http://dx.doi.org/10.1016/j.carbpol.2014.05.027

[15] H. Zhong, A. He, J. Lu, M. Sun, J. He, L. Zhang, J. Power Sources, (2016). http://dx.doi.org/10.1016/j.jpowsour.2016.10.041

[16] M. Mancini, F. Nobili, R. Tossici, R. Marassi, Electrochimica Acta, (2012). http://dx.doi.org/10.1016/j.electacta.2012.08.115

[17] T. Tanabe, Y. Liu, K. Miyamoto, Y. Irii, F. Maki, T. Gunji, S. Kaneko, S. Ugawa, H. Lee, T. Ohsaka, F. Matsumoto, Electrochimica Acta, (2017). https://doi.org/10.1016/j.electacta.2017.11.193

[18] X. Jia, Y. Kan, X. Zhu, G. Ning, Y. Lu, F. Wei, Nano Energ., (2014) http://dx.doi.org/10.1016/j.nanoen.2014.10.012

[19] W. Huang, J. Li, Y. Xu, Materials, 10, (2017).

[20] H. Chen, S. Zeng, M. Chen, Y. Zhang, Q. Li, Carbon, (2015). http://dx.doi.org/10.1016/j.carbon.2015.04.010

[21] Y. Cheng, Z. Chen, M. Zhu, Y. Lu, Adv. Energ. Mater., 5, (2014). https://doi.org/10.1002/aenm.201401207

[22] H. Fei, N. Saha, N. Kazantseva, R. Moučka, Q. Cheng, P. Saha, Materials, 10, (2017).

[23] X. Jia, Z. Chen, A. Suwarnasarn, L. Rice, X. Wang, H. Sohn, Q. Zhang, B.M. Wu, F. Wei, Y. Lu, Energ. Environ. Sci. 5, (2012).

[24] S. Luo, K. Wang, J. Wang, K. Jiang, Q. Li, S. Fan, Adv. Mater., 24, (2012). https://doi.org/10.1002/adma.201104720

[25] M. Frías, M.I. Sánchez de Rojas, M.P. Luxán, N.García, Cem. Concr. Res., (1991). http://dx.doi.org/10.1016/0008-8846(91)90165-E

[26] C. Wei, J. Shen, J. Zhang, H. Zhang, Ch. Zhu, RSC Adv. 4, (2014).

[27] Q. Feng, H. Kanoh, K. Ooi, J. Mater. Chem. 9, (1999)

[28] C. Julien, M. Massot, S. Rangan, M. Lemal, D. Guyomard, J. Raman Spectrosc., (2002). https://doi.org/10.1002/jrs.838

[29] B. Ammundsen, G.R. Burns, M.S. Islam, H. Kanoh, J. Roziere J. Phys. Chem. B, 103, (1999).

[30] M.M. Sinha, H.C. Gupta, Phys. B, 316-317, (2002).

[31] C.V. Ramana, M. Massot, C.M. Julien, Surf. Interface Anal., 37, (2005).

[32] E. G. Kelly, D.J. Spottiswood, The breakage function; What is it really? Minerals Engineering 3(5), (1990). https://doi.org/10.1016/0892-6875(90)90034-9

[33] A.N. Grundy, B. Hallstedt, L.J. Gauckler, J. Pha. Equilib. 24, (2003).

[34] Z. Zhang, Ch. Qu, T. Zheng, Y. Lai, J. Li, Int. J. Electrochem. Sci., 8, (2013).

[35] P. Randhawa, J.S. Park, S. Sharma, P. Kumar, M.S. Shin, S.S. Sekhon, J. Nanoelectron. Optoelectron. 7, (2012).

[36] W. Porcher, B. Lestriez, S. Jouanneau, D. Guyomard, J. Power Sources. 195, (2010).

[37] X. Wang, G. Shi, Energ. Environ. Sci., 8, (2015).

[38] J. Yan, J. Wang, H. Liu, Z. Bakenov, D. Gosselink, P. Chen, J. Power Sources 216, (2012)

[39] Y. Wang, J. Yi, Y. Xia, Adv. Energ. Mater., 2, (2012). https://doi.org/10.1002/aenm.201200065

[40] N. Alias, A.A. Mohamad, J. Power Sources., (2015) http://dx.doi.org/10.1016/j.jpowsour.2014.10.009

[41] Q. Li, J. Chen, L. Fan, X. Kong, Y. Lu, Green Energy & Environment 1,(2016) http://dx.doi.org/10.1016/j.gee.2016.04.006

[42] X. Zhu, X. Wu, T. N. L. Doan, Y. Tian, H. Zhao, P. Chen, J. Power Sources, (2016). https://doi.org/10.1016/j.jpowsour.2016.07.0029